

# Automatic selection of hyper-parameters via the use of softened profile likelihood

Gengyang Chen, Mu Zhu\*

Department of Statistics and Actuarial Science  
University of Waterloo  
Waterloo, Ontario, Canada N2L 3G1

November 4, 2025

## Abstract

We extend a heuristic method for automatic dimensionality selection, which maximizes a profile likelihood to identify “elbows” in scree plots. Our extension enables researchers to make automatic choices of multiple hyper-parameters simultaneously. To facilitate our extension to multi-dimensions, we propose a “softened” profile likelihood. We present two distinct parameterizations of our solution and demonstrate our approach on elastic nets, support vector machines, and neural networks. We also briefly discuss applications of our method to other data-analytic tasks than hyper-parameter selection.

---

\*This research is supported by grant RGPIN-2023-03337 from the Natural Sciences and Engineering Research Council (NSERC) of Canada.

# Contents

<b>1</b>	<b>Introduction</b>	<b>3</b>
<b>2</b>	<b>Methodology</b>	<b>4</b>
2.1	Brief review . . . . .	4
2.2	Generalization . . . . .	5
2.3	Softening . . . . .	5
2.4	Choice of $f$ . . . . .	6
2.5	Choice of $g$ and optimization tool . . . . .	7
2.5.1	Quadratic polynomial (QP) . . . . .	7
2.5.2	Two-layer neural network (2LNN) . . . . .	8
2.6	Further details . . . . .	8
2.6.1	Representative point on the boundary . . . . .	8
2.6.2	Transformation of optimization landscape . . . . .	9
<b>3</b>	<b>Examples</b>	<b>10</b>
3.1	Generalized elastic nets on Canadian temperature data . . . . .	10
3.2	Support vector machines on Parkinson data . . . . .	11
3.3	Neural networks on MNIST data . . . . .	14
<b>4</b>	<b>Discussion</b>	<b>17</b>
<b>5</b>	<b>Other applications</b>	<b>18</b>
<b>A</b>	<b>Derivation of Eq. (8)</b>	<b>20</b>
<b>B</b>	<b>Details of the MNIST example in Section 3.3</b>	<b>21</b>
B.1	Details about dropout . . . . .	21
B.2	Other details . . . . .	21
<b>C</b>	<b>Details of other applications in Section 5</b>	<b>22</b>

# 1 Introduction

Researchers who use computational tools often look at a so-called “scree plot” to make choices about certain hyper-parameters in their numeric procedure. Figure 1a shows a prototypical scenario: A team of researchers may be training a model while using a certain hyper-parameter to penalize its complexity. When the penalty is small, relatively low training errors can be achieved, but the researchers understand the model is likely overfitting the training data. As the penalty is increased, the error grows as well. The growth is slow and steady at first, but becomes much steeper “at some point”—here, marked by a dashed vertical line in Figure 1a. It is this “turning point” that is critical to the researchers. For example, they may conclude that the reduction in model complexity “up to this point” will more than compensate for the slight increase in training error, but that any continued reduction “beyond this point” will no longer be justifiable against the sharp increase in error.

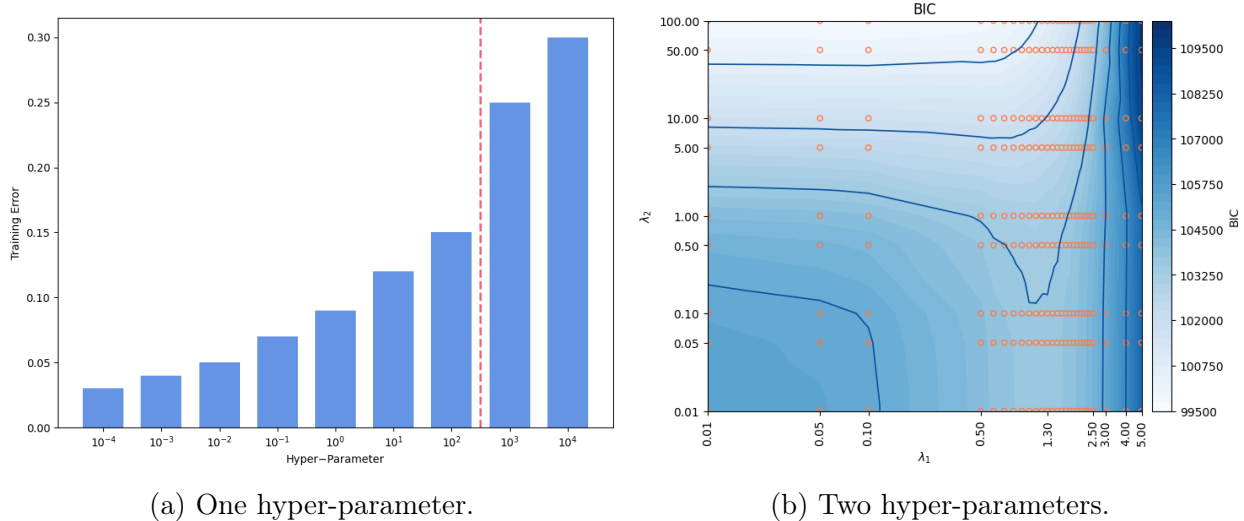


Figure 1: Examples of hyper-parameters affecting model performance.

Zhu and Ghodsi (2006) provided a heuristic method to automate such decisions. The need for automation is most prominent when running repeated simulations. Without an automatic procedure, researchers would have to stop each simulation in the middle to inspect the “scree plot” before an appropriate hyper-parameter can be chosen and the simulation can be continued. Over the past two decades, their method has garnered reasonably wide attention and adoption by researchers from different fields, such as bioinformatics (e.g., Fogel et al., 2007), demographics (e.g., Zhong et al., 2021), ecology (e.g., Hamady et al., 2010), genetics (e.g., Lai et al., 2009), geoscience (e.g., Honarkhah and Caers, 2010), and physics (e.g., Chang et al., 2022). It has also become a frequently used tool in network data analysis (e.g., Lyzinski et al., 2017), the study of random graphs (e.g., Tang et al., 2017), and spectral clustering (e.g., Priebe et al., 2019).

Although it can be used generally for hyper-parameter selection, the heuristic method of Zhu and Ghodsi (2006) was originally presented for the purpose of determining the number of

principal components, and not applicable to problems with more than one hyper-parameter; we will elaborate on this limitation later in Section 2.2 to make it more clear.

On the other hand, it is now common for many statistical and computational problems to have more than one hyper-parameter. A highly-cited example in statistics is the elastic net (Zou and Hastie, 2005):

$$\min_{\boldsymbol{\beta}} \|\mathbf{y} - \mathbf{X}\boldsymbol{\beta}\|_{\ell_2}^2 + \lambda_1 \|\boldsymbol{\beta}\|_{\ell_1} + \lambda_2 \|\mathbf{D}\boldsymbol{\beta}\|_{\ell_2}^2 \quad (1)$$

with two hyper-parameters  $\lambda_1, \lambda_2 > 0$ . The original elastic net constrains  $\mathbf{D} = \mathbf{I}$  to be the identity matrix; the version we have given above is sometimes referred to as the “generalized” elastic net (GEN). Figure 1b shows an example of fitting a GEN model (1) to hourly temperature measurements collected from 13 weather stations across Canada during the month of July between 2019 and 2022. We will return to this example in Section 3.1 with more details, but the decision faced here by the data analyst can already be appreciated: Initially as both hyper-parameters increase, the evaluation metric decreases—here, meaning the model is judged more favorably. The metric decreases steadily at first in both directions, but “at some point” the metric starts to decrease much more slowly in the  $\lambda_2$ -direction and even starts to increase in the  $\lambda_1$ -direction.

The method of Zhu and Ghodsi (2006) can be used to determine the “turning point” in Figure 1a, but not the one in Figure 1b. In this article, we extend their work to overcome this limitation.

## 2 Methodology

In a nutshell, our primary objective is to develop a method for identifying a boundary in the space of hyper-parameters at which improvements in model performance can be considered to have plateaued. Specifically, we aim to estimate a boundary curve—say,  $g(\mathbf{u}; \boldsymbol{\omega}) = 0$ —and a representative point on it, from a dataset of  $n$  performance evaluations  $\{(\mathbf{u}_i, z_i)\}_{i=1}^n$ , where each  $\mathbf{u}_i$  denotes a specific hyper-parameter configuration and  $z_i$ , the corresponding value of model performance. Our methodology involves constructing a model for  $z_i$  and estimating the boundary curve by maximizing a profile log-likelihood function. We also provide a principled procedure for selecting a representative point on this boundary, and recommend a simple transformation of  $\mathbf{u}_i$  in practice to improve numerical stability during optimization.

### 2.1 Brief review

We start with a brief summary of Zhu and Ghodsi (2006). Suppose  $u_1, u_2, \dots, u_n$  are a set of candidate values for a hyper-parameter, and  $z_1, z_2, \dots, z_n$  are the corresponding values of an evaluation metric under consideration. Their idea is to model each  $z_i$  as an independent

observation from either of two different distributions depending on whether  $u_i$  is above or below a certain threshold  $\omega$ , i.e.,

$$z_i \sim \begin{cases} f(z; \boldsymbol{\theta}_1), & \text{if } u_i \leq \omega; \\ f(z; \boldsymbol{\theta}_2), & \text{if } u_i > \omega. \end{cases}$$

The log-likelihood is then given by

$$\ell(\omega, \boldsymbol{\theta}_1, \boldsymbol{\theta}_2) = \sum_{u_i \leq \omega} \log f(z_i; \boldsymbol{\theta}_1) + \sum_{u_i > \omega} \log f(z_i; \boldsymbol{\theta}_2),$$

and the optimal threshold is chosen by maximizing the profile log-likelihood,

$$\ell_\omega(\omega) = \sum_{u_i \leq \omega} \log f(z_i; \hat{\boldsymbol{\theta}}_1(\omega)) + \sum_{u_i > \omega} \log f(z_i; \hat{\boldsymbol{\theta}}_2(\omega)), \quad (2)$$

where  $\hat{\boldsymbol{\theta}}_j(\omega)$  is the maximum likelihood estimator (MLE) of  $\boldsymbol{\theta}_j$  for any given  $\omega$ , with  $j \in \{1, 2\}$ .

## 2.2 Generalization

If we have more than one hyper-parameter, then  $\mathbf{u}_1, \mathbf{u}_2, \dots, \mathbf{u}_n \in \mathbb{R}^m$  with  $m > 1$ . Clearly, this multidimensional space can no longer be separated into two regions by a simple threshold. That is why the method of Zhu and Ghodsi (2006) no longer applies. Instead, we will need a “boundary function”, say,  $g(\mathbf{u}; \boldsymbol{\omega})$ , parameterized here by  $\boldsymbol{\omega}$ ; it will partition the space into

$$\{\mathbf{u} \in \mathbb{R}^m : g(\mathbf{u}; \boldsymbol{\omega}) \leq 0\} \quad \text{and} \quad \{\mathbf{u} \in \mathbb{R}^m : g(\mathbf{u}; \boldsymbol{\omega}) > 0\},$$

depending on which side of the boundary  $\mathbf{u}$  lies. Conceptually, we can simply obtain the optimal boundary by maximizing a similar profile log-likelihood,

$$\ell_{\boldsymbol{\omega}}(\boldsymbol{\omega}) = \sum_{g(\mathbf{u}_i; \boldsymbol{\omega}) \leq 0} \log f(z_i; \hat{\boldsymbol{\theta}}_1(\boldsymbol{\omega})) + \sum_{g(\mathbf{u}_i; \boldsymbol{\omega}) > 0} \log f(z_i; \hat{\boldsymbol{\theta}}_2(\boldsymbol{\omega})), \quad (3)$$

completely analogous to Eq. (2). In particular, Eq. (2) is easily seen to be a special case of Eq. (3), with  $g(u; \omega) = u - \omega$  and  $u, \omega \in \mathbb{R}$ . However, because Eq. (3) is not a continuous function of  $\boldsymbol{\omega}$ , some further modification is needed (details in Section 2.3 below) to make the optimization problem practical to solve.

## 2.3 Softening

Since Zhu and Ghodsi (2006) only dealt with the one-dimensional case of  $u_i \in \mathbb{R}$ , a direct grid search—typically just over the entire set of candidate values  $\{u_1, u_2, \dots, u_n\}$ —was sufficient

in practice for them to maximize Eq. (2) over  $\omega$ . For  $\mathbf{u}_i \in \mathbb{R}^m$  with  $m > 1$ , such an approach is no longer applicable, and we will need to use numerical optimization tools to maximize Eq. (3) over  $\omega$ , but the fact that Eq. (3) is not continuous in  $\omega$  poses an extra challenge.

Our main idea here is to turn Eq. (3) into a continuous function of  $\omega$  by replacing the “hard” assignment of each  $\mathbf{u}_i$  to one side of the boundary, i.e.,

$$\text{either } g(\mathbf{u}_i; \omega) \leq 0 \quad \text{or} \quad g(\mathbf{u}_i; \omega) > 0,$$

with a “soft” weight based on the sigmoid function,

$$s_i(\omega) := \frac{1}{1 + \exp(-g(\mathbf{u}_i; \omega))}, \quad (4)$$

which is close to zero if  $\mathbf{u}_i$  is on one side of the boundary  $g(\mathbf{u}_i; \omega) \leq 0$ , and close to one if it is on the other side  $g(\mathbf{u}_i; \omega) > 0$ .

More specifically, the “softened” profile log-likelihood becomes

$$\ell_{\omega}^{\text{soft}}(\omega) = \sum_{i=1}^n (1 - s_i(\omega)) \log f(z_i; \hat{\theta}_1^{\text{soft}}(\omega)) + \sum_{i=1}^n s_i(\omega) \log f(z_i; \hat{\theta}_2^{\text{soft}}(\omega)), \quad (5)$$

where

$$(\hat{\theta}_1^{\text{soft}}(\omega), \hat{\theta}_2^{\text{soft}}(\omega)) = \arg \max_{(\theta_1, \theta_2)} \left\{ \sum_{i=1}^n (1 - s_i(\omega)) \log f(z_i; \theta_1) + \sum_{i=1}^n s_i(\omega) \log f(z_i; \theta_2) \right\}, \quad (6)$$

are “softened” MLEs given  $\omega$ . One can easily see that both the original profile log-likelihood (3) and the “usual” MLEs given  $\omega$ ,

$$(\hat{\theta}_1(\omega), \hat{\theta}_2(\omega)) = \arg \max_{(\theta_1, \theta_2)} \left\{ \sum_{g(\mathbf{u}_i; \omega) \leq 0} \log f(z_i; \theta_1) + \sum_{g(\mathbf{u}_i; \omega) > 0} \log f(z_i; \theta_2) \right\},$$

are simply special cases of (5) and (6), respectively, with

$$s_i(\omega) = \begin{cases} 0, & g(\mathbf{u}_i; \omega) \leq 0; \\ 1, & g(\mathbf{u}_i; \omega) > 0 \end{cases}$$

being a step function, which is what caused the discontinuity problem mentioned earlier at the end of Section 2.2.

## 2.4 Choice of $f$

Zhu and Ghodsi (2006) assumed

$$f(z; \theta_j) := f(z; \mu_j, \sigma^2) = \frac{1}{\sqrt{2\pi\sigma^2}} \exp \left\{ -\frac{(z - \mu_j)^2}{2\sigma^2} \right\}, \quad j \in \{1, 2\}. \quad (7)$$

That is, the two different distributions were assumed to be Gaussian with a different mean but a common variance.

This was the most arbitrary assumption in their work, but also what allowed their automatic procedure to produce threshold choices in one dimension that best “matched” what an “average” data scientist would otherwise choose by visual inspection. Therefore, we shall keep this assumption in this article. Examples later in Section 3 will confirm that doing so does indeed allow us to produce boundaries that *continue* to “match” what an “average” data scientist would otherwise sketch out in the space of  $\mathbf{u}_1, \mathbf{u}_2, \dots, \mathbf{u}_n$  by visual inspection.

Straightforward derivations omitted here but provided in Appendix A will now allow us to conclude that, under assumption (7), the “softened” profile log-likelihood (5) can be further reduced to

$$\ell_{\boldsymbol{\omega}}^{\text{soft}}(\boldsymbol{\omega}) = -\frac{n}{2} \log(2\pi\hat{\sigma}^2(\boldsymbol{\omega})) - \frac{n}{2}, \quad (8)$$

where

$$\hat{\sigma}^2(\boldsymbol{\omega}) = \frac{\text{RSS}_1(\boldsymbol{\omega}) + \text{RSS}_2(\boldsymbol{\omega})}{n},$$

with

$$\text{RSS}_1(\boldsymbol{\omega}) = \sum_{i=1}^n (1 - s_i(\boldsymbol{\omega}))(z_i - \hat{\mu}_1(\boldsymbol{\omega}))^2, \quad \text{RSS}_2(\boldsymbol{\omega}) = \sum_{i=1}^n s_i(\boldsymbol{\omega})(z_i - \hat{\mu}_2(\boldsymbol{\omega}))^2,$$

and

$$\hat{\mu}_1(\boldsymbol{\omega}) = \frac{\sum_{i=1}^n (1 - s_i(\boldsymbol{\omega}))z_i}{\sum_{i=1}^n (1 - s_i(\boldsymbol{\omega}))}, \quad \hat{\mu}_2(\boldsymbol{\omega}) = \frac{\sum_{i=1}^n s_i(\boldsymbol{\omega})z_i}{\sum_{i=1}^n s_i(\boldsymbol{\omega})}.$$

Thus, in practice our procedure simply amounts to maximizing Eq. (8) over  $\boldsymbol{\omega}$ .

## 2.5 Choice of $g$ and optimization tool

We consider two distinct parameterizations of the boundary function  $g(\mathbf{u}; \boldsymbol{\omega})$  and use different optimization tools for each.

### 2.5.1 Quadratic polynomial (QP)

A natural and interpretable choice for modeling a boundary function is a second-degree polynomial such as

$$g(\mathbf{u}; \boldsymbol{\omega}) = \mathbf{u}^\top \mathbf{A} \mathbf{u} + \mathbf{b}^\top \mathbf{u} + c, \quad (9)$$

with  $\boldsymbol{\omega} = \{\mathbf{A}, \mathbf{b}, c\}$ . For  $\mathbf{u} \equiv (x, y)^\top \in \mathbb{R}^2$ , this simplifies to

$$g(x, y; \boldsymbol{\omega}) = ax^2 + bxy + cy^2 + dx + ey + f,$$

with  $\boldsymbol{\omega} = (a, b, c, d, e, f) \in \mathbb{R}^6$  now being a vector of six real-valued coefficients.

This parameterization is expressive enough to represent various boundary shapes and can be interpreted geometrically as a conic section, while still maintaining simplicity. When the goal is to preserve model simplicity, interpretability, and convexity, this choice is particularly suitable.

Since the boundary function  $g(\mathbf{u}; \boldsymbol{\omega})$  is differentiable with respect to its parameters and lies in a relatively low-dimensional space, we adopt the quasi-Newton method BFGS (e.g., Nocedal and Wright, 2006, p. 136) to optimize the profile log-likelihood.

### 2.5.2 Two-layer neural network (2LNN)

To accommodate more flexible boundary shapes, we can also parameterize the boundary function using a shallow neural network such as

$$g(\mathbf{u}; \boldsymbol{\omega}) = \mathbf{w}_2^\top \tanh(\mathbf{W}_1 \mathbf{u} + \mathbf{b}_1) + b_2, \quad (10)$$

with  $\boldsymbol{\omega} = \{\mathbf{W}_1, \mathbf{b}_1, \mathbf{w}_2, b_2\}$  being the entire set of trainable parameters (i.e., weights and biases). In our current implementation, we use a fully-connected network with one hidden layer of size 32, i.e.,  $\mathbf{W}_1 \in \mathbb{R}^{32 \times m}$ ,  $\mathbf{b}_1 \in \mathbb{R}^{32}$ ,  $\mathbf{w}_2 \in \mathbb{R}^{32}$ , and  $b_2 \in \mathbb{R}$ . For example, if  $\mathbf{u} \in \mathbb{R}^2$ , this leads to an optimization problem in  $32 \times 2 + 32 + 32 + 1 = 129$  dimensions.

This structure introduces nonlinearity through the activation function  $\tanh(\cdot)$ , enabling the boundary curve to capture complex, non-convex geometries beyond the capacity of a quadratic form. Given the increased number of parameters even for  $\mathbf{u} \in \mathbb{R}^2$  and the added non-convexity of  $g$  itself, we employ the ADAM optimizer (Kingma and Ba, 2014) for training.

## 2.6 Further details

We now discuss some further practical details. While all our discussions here are applicable to  $\mathbf{u}_i \in \mathbb{R}^m$  for any  $m > 1$ , to reduce notational clutter such as additional superscripts and subscripts we will restrict  $\mathbf{u}_i \equiv (x_i, y_i)^\top \in \mathbb{R}^2$  to be two-dimensional in this section.

### 2.6.1 Representative point on the boundary

While all points on the estimated boundary curve  $g(x, y; \hat{\boldsymbol{\omega}}) = 0$  are theoretically equivalent in identifying the beginning of performance plateau, there may be practical situations where selecting a single representative point is desirable.

To determine such a point in a principled manner, we propose an additional heuristic based on the notion of the center of gravity (COG) from classical mechanics. This approach requires that all performance values  $z_i$  have the same sign, which can be ensured through a suitable

shift if necessary. Under this assumption, we interpret  $|z_i|$  as the “mass” located at the point  $(x_i, y_i)$  in the parameter space.

**Definition 1** (Center of Gravity (COG)). Let the index sets be defined as

$$\mathcal{I}_1 := \{i : g(x_i, y_i; \hat{\omega}) \leq 0\}, \quad \mathcal{I}_2 := \{i : g(x_i, y_i; \hat{\omega}) > 0\}.$$

Then, the center of gravity (COG) in region  $\mathcal{I}_j$ , for  $j \in \{1, 2\}$ , is the point  $(x_{\text{COG}}^{(j)}, y_{\text{COG}}^{(j)})$ , where

$$x_{\text{COG}}^{(j)} = \frac{\sum_{i \in \mathcal{I}_j} x_i |z_i|}{\sum_{i \in \mathcal{I}_j} |z_i|} \quad \text{and} \quad y_{\text{COG}}^{(j)} = \frac{\sum_{i \in \mathcal{I}_j} y_i |z_i|}{\sum_{i \in \mathcal{I}_j} |z_i|} \quad (11)$$

are weighted averages of  $\{(x_i, y_i) : i \in \mathcal{I}_j\}$  using  $|z_i|$  as mass.  $\square$

We then connect the two centers of gravity,  $(x_{\text{COG}}^{(1)}, y_{\text{COG}}^{(1)})$  and  $(x_{\text{COG}}^{(2)}, y_{\text{COG}}^{(2)})$ , with a straight line. The intersection point  $(x_b, y_b)$  of this line with the boundary curve  $g(x, y; \hat{\omega}) = 0$  is selected as the representative point.

In practice, it may sometimes be preferable to identify a “best” point in the original grid, i.e., one of  $\{(x_i, y_i)\}_{i=1}^n$ , rather than the interpolated boundary point  $(x_b, y_b)$ , especially when downstream tasks may require using a model configuration  $(x_i, y_i)$  that has already been explicitly evaluated. In such cases, users can simply choose the nearest grid point to  $(x_b, y_b)$ , i.e.,

$$(x_b^\dagger, y_b^\dagger) = \arg \min_i \|(x_i, y_i) - (x_b, y_b)\|. \quad (12)$$

This ensures the selected point is both practically usable and as close as possible to the representative boundary point. One can also restrict the choice to the “good side” of the boundary, say  $\mathcal{I}_j$ , and take the “ $\arg \min$ ” above over  $i \in \mathcal{I}_j$  alone rather than over all  $i$ , but such restriction is not necessary.

### 2.6.2 Transformation of optimization landscape

In practical applications, the hyper-parameters  $(x_i, y_i)$  may exhibit significant skewness or lie on widely different scales. Such disparities in scale can induce a distorted and ill-conditioned geometry in the optimization landscape, potentially hindering the convergence of gradient-based optimizers.

To address these issues, we recommend to apply a convenient yet effective data transformation to each parameter dimension. The transformation consists of a logarithmic scaling—used to compress large values and reduce skewness—followed by standard normalization to produce zero-mean, unit-variance features:

$$x_i \leftarrow \frac{\log x_i - \overline{\log x}}{\text{SD}(\log x)}, \quad y_i \leftarrow \frac{\log y_i - \overline{\log y}}{\text{SD}(\log y)}, \quad (13)$$

where  $\overline{\log x}$  and  $\text{SD}(\log x)$  denote the sample mean and standard deviation of the log-transformed  $x_i$  values (and similarly for  $y_i$ ) over all  $i \in \{1, 2, \dots, n\}$ . This preprocessing step helps regularize the parameter space and promotes numerically stable optimization.

### 3 Examples

We now illustrate the usefulness of our method using real-world examples across a diverse set of modeling contexts, including generalized elastic nets for climate data, support vector machines for detecting Parkinson’s disease, and neural networks for image recognition. Although in Section 2 we have presented our method generally for  $m > 1$ , in reality it is rare for researchers to experimentally decide on more than two hyper-parameters due to the exponential increase in computational cost. The most common practice is to rely on experiments for the two most important—or most sensitive—hyper-parameters, while fixing all others at some pre-determined values. Thus in this section, we will consider only two hyper-parameters in all cases as well, i.e.,  $\mathbf{u} = (x, y) \in \mathbb{R}^2$ ; this also makes it easier to examine the results visually. We will display contours of the performance metric, together with the boundary curve  $g(x, y; \hat{\boldsymbol{\omega}}) = 0$  computed by our method, the center of gravity on either side of the boundary, and the representative boundary point, etc. Table 1 summarizes the legend we use in all of our figures.

Legend	Description (refer to Section 2.6.1)
+	center of gravity $(x_{\text{COG}}^{(j)}, y_{\text{COG}}^{(j)})$ in $\mathcal{I}_j$ , for either $j \in \{1, 2\}$
$\times$	representative boundary point $(x_b, y_b)$
$\Upsilon$	point $(x_b^\dagger, y_b^\dagger)$ in $\mathcal{I}_1$ that is nearest to $(x_b, y_b)$
$\curlywedge$	point $(x_b^\dagger, y_b^\dagger)$ in $\mathcal{I}_2$ that is nearest to $(x_b, y_b)$

Table 1: Summary of legend used in Figures 2, 3 and 4.

#### 3.1 Generalized elastic nets on Canadian temperature data

Our first example is taken from Jian et al. (2024, Section 5). Among other things, they fitted a GEN model (1) to some Canadian temperature data, which we have already introduced briefly in Section 1. The set-up of their model and the exact meanings of their  $\mathbf{y}$ ,  $\mathbf{X}$ ,  $\mathbf{D}$  and  $\boldsymbol{\beta}$  are quite involved, as they were using regression techniques to estimate partial correlation coefficients of temperature measurements between different locations as they change over the 24-hour period of the day. We will not go into these details as they are irrelevant to our discussion here. It suffices for us to state that, in their context, the  $\ell_1$ -penalty in Eq. (1) encourages some of those partial correlation coefficients to be zero, while the  $\ell_2$ -penalty encourages all the partial correlation coefficients to change smoothly over time.

For model evaluation they used the Bayesian information criterion (BIC), defined in such a way that lower values are favored, but they had difficulties with how to choose the two hyper-parameters because many different  $(\lambda_1, \lambda_2)$ -pairs resulted in similarly low BIC values and it was not clear if any particular pair was more favorable than others. They ended up choosing two different sets of hyper-parameters and argued that using either set led to the same underlying scientific conclusions (see Jian et al., 2024, Section 5, p. 868).

Figure 1b is produced with information they shared with us—specifically, different  $(\lambda_1, \lambda_2)$ -pairs they considered for their data and the resulting BIC values that corresponded to each pair. The aforementioned difficulty which they faced is readily visible from this plot. Figure 2 shows the boundaries that our method is able to find for this example, when the boundary itself is parameterized either as a QP (Figure 2a) or as a 2LNN (Figure 2b). Also shown in the plots are the center of gravity on either side of the boundary (labeled “+”) and the representative boundary point (labeled “ $\times$ ”), which would be our choice if we were acting as consultants for the study—except that we would further round up the answer to  $(\lambda_1, \lambda_2) = (1.0, 2.0)$  out of practical considerations.

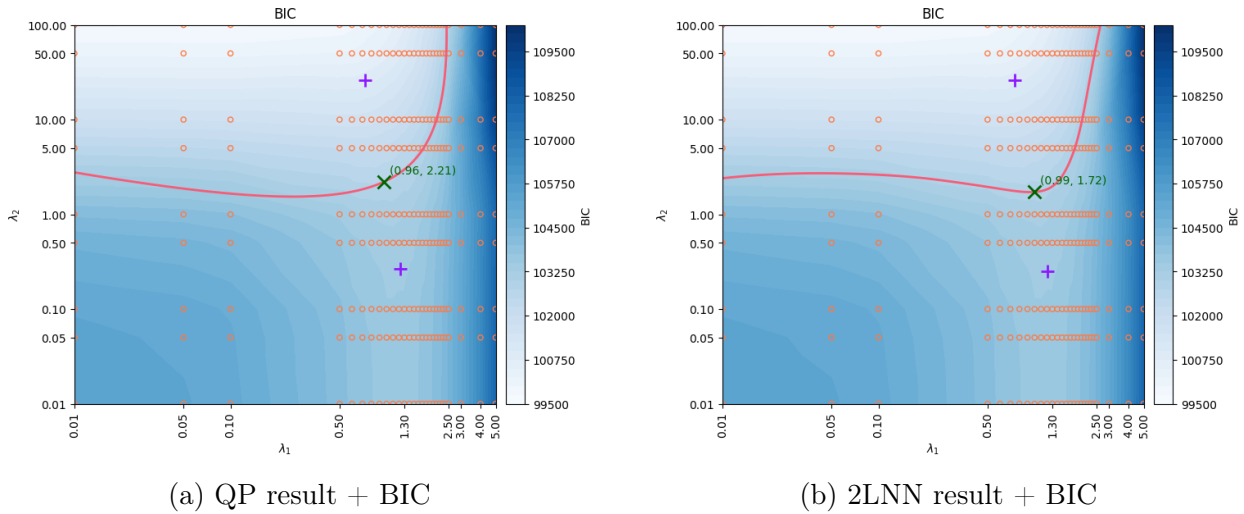


Figure 2: Bayesian information criterion on the Canadian temperature dataset as a function of two hyper-parameters,  $\lambda_1$  and  $\lambda_2$ ; see Eq. (1).

### 3.2 Support vector machines on Parkinson data

Our next example concerns the support vector machine (SVM; see, e.g., Cortes and Vapnik, 1995), a method which dominated the field of machine learning during much of the two decades before the deep learning movement came into full swing.

Here, we use it to detect the presence of Parkinson’s disease (PD) from acoustic features of voice recordings. The dataset originates from Sakar et al. (2013) and is available in the UCI Machine Learning Repository under the title, “Parkinson’s Speech with Multiple Types of Sound Recordings”. It comprises a training set of 1,040 voice samples (sustained vowels, numbers, words, and short sentences), with equal numbers from PD patients and healthy individuals. From each sample, 26 linear and time-frequency based features (e.g., pitch-related measures, number of pulses, degree of voice breaks) are extracted. A separate test set of 168 voice samples that was collected independently under the same clinical protocol provides held-out data for validation.

1. Solve

$$\begin{aligned} \max_{\alpha_1, \dots, \alpha_N} \quad & \sum_{i=1}^N \alpha_i - \frac{1}{2} \sum_{i=1}^N \sum_{j=1}^N \alpha_i \alpha_j y^{(i)} y^{(j)} K_h(\mathbf{x}^{(i)}; \mathbf{x}^{(j)}) \\ \text{s.t.} \quad & \sum_{i=1}^N \alpha_i y^{(i)} = 0, \\ & 0 \leq \alpha_i \leq \gamma, \quad \forall i \in \{1, 2, \dots, N\}. \end{aligned}$$

2. Based on the solutions  $\alpha_1, \dots, \alpha_N$  to Step 1, partition the set  $\{1, 2, \dots, N\}$  into three disjoint groups:

$$G_0 \equiv \{i : \alpha_i = 0\}, \quad G_\gamma \equiv \{i : \alpha_i = \gamma\}, \quad G_{(0, \gamma)} \equiv \{i : 0 < \alpha_i < \gamma\}.$$

3. Pick any  $i \in G_{(0, \gamma)}$ , and solve

$$\alpha_0 = y^{(i)} - \sum_{j=1}^N \alpha_j y^{(j)} K_h(\mathbf{x}^{(i)}; \mathbf{x}^{(j)}).$$

Table 2: The key steps to fit an SVM for binary classification ( $y^{(i)} = \pm 1$ ), given fixed hyper-parameters  $h$  and  $\gamma$ .

Given a training dataset  $\{(\mathbf{x}^{(i)}, y^{(i)})\}_{i=1}^N$ , where  $y^{(i)} = \pm 1$  is a binary label, the SVM classifies a new point  $\mathbf{x}$  by the sign of

$$p(\mathbf{x}) = \sum_{i=1}^N \alpha_i y^{(i)} K_h(\mathbf{x}; \mathbf{x}^{(i)}) + \alpha_0, \quad (14)$$

where  $K_h(\cdot; \cdot)$  is a pre-specified kernel function with hyper-parameter  $h$ , and  $\alpha_0, \alpha_1, \dots, \alpha_N$  are obtained by following the steps given in Table 2, which involve an additional hyper-parameter  $\gamma$ . These steps are nontrivial to explain, but we will spare the readers from such details as they are not directly pertinent to our discussion.

We use the radial basis kernel,

$$K_h(\mathbf{u}; \mathbf{v}) = \exp \{-h\|\mathbf{u} - \mathbf{v}\|^2\},$$

and the **svm** function from the R package **e1071** to fit (14). The left side of Figure 3 shows the classification error (in %) on the training examples as the two hyper-parameters  $(h, \gamma)$  vary. The training error starts relatively low in the top-right corner when both  $(h, \gamma)$  are relatively large, but these SVMs are overfitting the training data. As their values are decreased, the training error increases, gradually at first but more sharply “at some point”.

The left side of the figure also shows the boundaries marking the beginning of these sharp increases as determined by our method, when the boundary itself is parameterized either

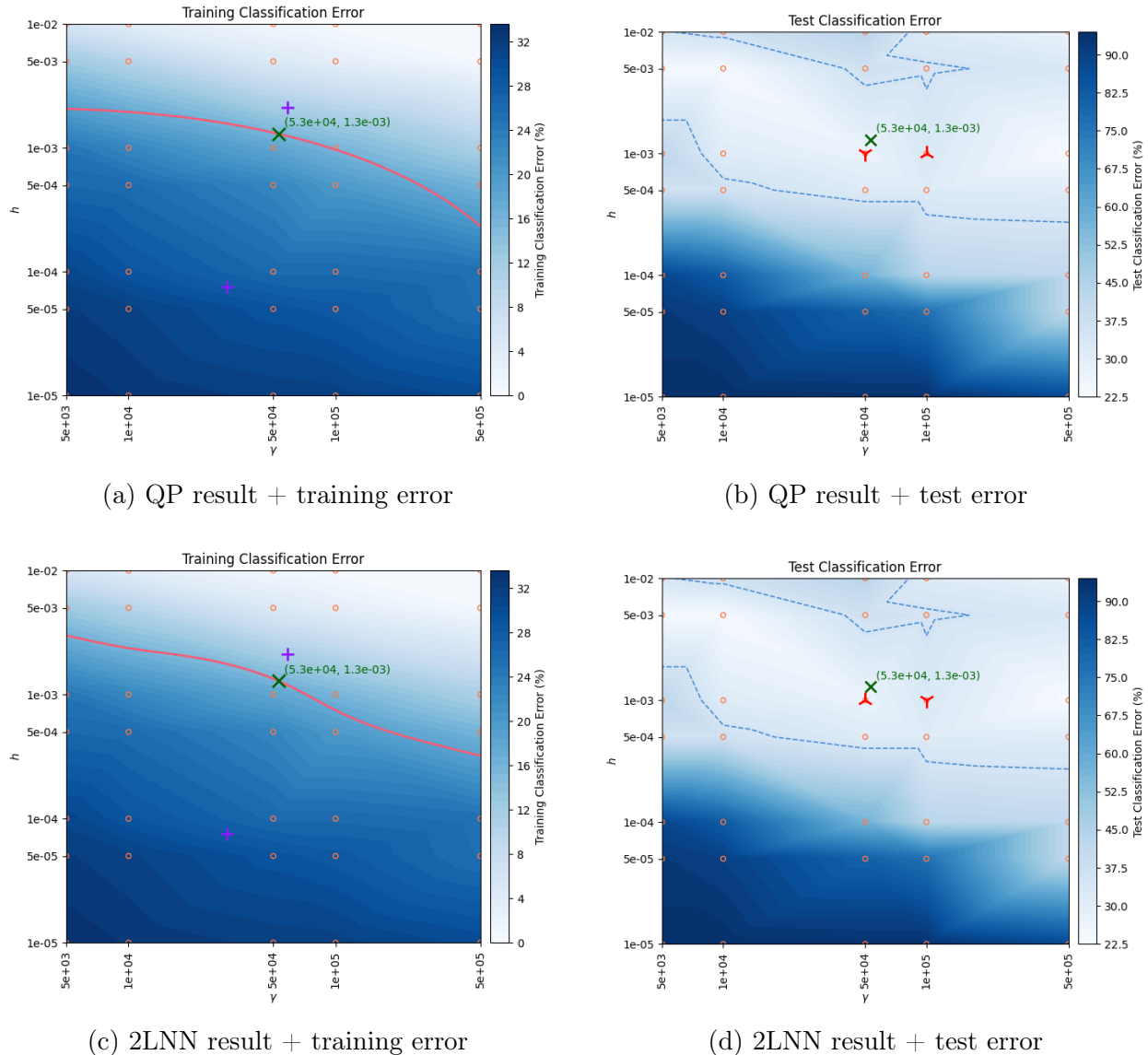


Figure 3: Classification error (in %) on the Parkinson dataset as a function of two hyper-parameters,  $\gamma$  and  $h$ ; see Table 2.

as a QP (Figure 3a) or as a 2LNN (Figure 3c). Regardless of which parameterization, our method suggests that  $h$  should be no less than about  $1 \times 10^{-3}$  and that  $\gamma$  should be no less than about  $5 \times 10^4$ ; it also finds almost the same representative boundary point at roughly  $(\gamma_b, h_b) = (5.3 \times 10^4, 1.3 \times 10^{-3})$ , labeled “ $\times$ ” in all panels of Figure 3.

The right side of Figure 3 shows the classification error (again, in %) on the 168 held-out samples. As expected, the error surface is noisier on held-out data, but it is reassuring to see that the representative boundary point at roughly  $(\gamma_b, h_b) = (5.3 \times 10^4, 1.3 \times 10^{-3})$  clearly corresponds to an SVM which would have a favorably low test error. Although such an SVM has not been fitted, among those already fitted the “closest” one is at  $(\gamma_b^\dagger, h_b^\dagger) = (5 \times 10^4, 1 \times 10^{-3})$ . Its test error of about 27.38% is indeed among the lowest of all SVMs fitted. In Figures 3b and 3d, it is labeled “ $\Upsilon$ ” and “ $\lambda$ ”, respectively.

### 3.3 Neural networks on MNIST data

Our final example is an application of our method to selecting hyper-parameters when training neural networks, based on the paper by Srivastava et al. (2014). In the rapidly evolving field of deep learning, this paper is considered an early contribution but it remains an influential classic for popularizing the so-called “dropout” technique, whose combination with another procedure called “max-norm regularization” was found to be especially effective at reducing generalization error (Srivastava et al., 2014, Section 6.5).

To illustrate, we use the well-known MNIST dataset, which contains 60,000 training examples and 10,000 test examples, each representing a  $28 \times 28$  grayscale image of a handwritten digit. The classification task is to assign each image to one of the ten digit classes,  $\{0, 1, \dots, 9\}$ .

We use a stochastic gradient descent algorithm (Table 3) with both dropout (Step 2 of Table 3) and max-norm regularization (Step 4 of Table 3) to train a neural network  $\mathbf{p}(\mathbf{x})$  by the cross-entropy loss function,

$$L(y, \mathbf{p}(\mathbf{x})) = -\log(p_y(\mathbf{x})), \quad y \in \{1, 2, \dots, K\},$$

where  $p_k(\mathbf{x})$  denotes the  $k$ -th element of  $\mathbf{p}(\mathbf{x}) \in (0, 1)^K$ . Statisticians may simply know this loss function better as the negative multinomial log-likelihood. For  $\mathbf{p}(\mathbf{x})$ , we use one of the architectures considered by Srivastava et al. (2014, Section 6.1) with two hidden layers (more details in Appendix B),

$$\mathbf{p}(\mathbf{x}) = \sigma [\mathbf{W}_3 \rho \{ \mathbf{W}_2 \rho (\mathbf{W}_1 \mathbf{x} + \mathbf{b}_1) + \mathbf{b}_2 \} + \mathbf{b}_3], \quad (15)$$

where  $\rho(\mathbf{z}) = \max(\mathbf{0}, \mathbf{z})$  is the ReLU activation function applied element-wise, and

$$\sigma(z_1, \dots, z_K) = \frac{1}{(e^{z_1} + \dots + e^{z_K})} (e^{z_1}, \dots, e^{z_K})$$

is the softmax function that maps  $\mathbb{R}^K$  to  $(0, 1)^K$ . For the MNIST data,  $K = 10$  and  $\mathbf{x} \in \mathbb{R}^{784}$ .

Initialize  $\boldsymbol{\theta} := \{\mathbf{W}_1, \mathbf{W}_2, \mathbf{W}_3, \mathbf{b}_1, \mathbf{b}_2, \mathbf{b}_3\}$  (more details in Appendix B.2) and set  $\mathbf{m}_0 \leftarrow \mathbf{0}$ .

For  $t = 1, \dots, T$ :

1. Sample a mini-batch  $\{(\mathbf{x}^{(i)}, y^{(i)})\}_{i=1}^B$  from the training dataset  $\mathcal{D}$ .
2. Calculate  $\mathbf{g}_t \leftarrow \nabla_{\boldsymbol{\theta}} \tilde{L}_t(\boldsymbol{\theta}_{t-1})$ , where

$$\tilde{L}_t(\boldsymbol{\theta}) = \frac{1}{B} \sum_{i=1}^B L \left( y^{(i)}, \mathbb{D}_t^{(i)}[\mathbf{p}(\mathbf{x}^{(i)}; \boldsymbol{\theta}); r] \right)$$

and  $\mathbb{D}_t^{(i)}(\cdot; r)$  is a stochastic operation which, for every  $i$  and  $t$ , randomly “drops out” a set of nodes in its neural network argument and rescales the remaining ones (more details in Appendix B.1). (This makes  $\mathbf{g}_t$  here slightly different from  $\nabla_{\boldsymbol{\theta}} L_t(\boldsymbol{\theta}_{t-1})$ , where

$$L_t(\boldsymbol{\theta}) = \frac{1}{B} \sum_{i=1}^B L \left( y^{(i)}, \mathbf{p}(\mathbf{x}^{(i)}; \boldsymbol{\theta}) \right)$$

is the “usual” average loss over the mini-batch.)

3. Update

$$\mathbf{m}_t \leftarrow \mu_t \mathbf{m}_{t-1} + \mathbf{g}_t \quad \text{and} \quad \boldsymbol{\theta}_t \leftarrow \boldsymbol{\theta}_{t-1} - \epsilon_t \mathbf{m}_t$$

where  $\mu_t$  and  $\epsilon_t$  each follow a pre-specified schedule over  $t$  (more details in Appendix B.2).

4. Rescale each row,  $\mathbf{w}_j$ , of  $\mathbf{W}_1, \mathbf{W}_2, \mathbf{W}_3 \in \boldsymbol{\theta}_t$  by

$$\mathbf{w}_j \leftarrow \mathbf{w}_j \cdot \min \left( 1, \frac{c}{\|\mathbf{w}_j\|_2 + \varepsilon} \right), \quad \varepsilon = 10^{-7}.$$

End For

Table 3: Training the neural network in Eq. (15) using a stochastic gradient descent algorithm with both dropout (the  $\mathbb{D}_t^{(i)}$  operator with dropout rate  $r$  in Step 2) and max-norm regularization (the  $c$  parameter in Step 4).

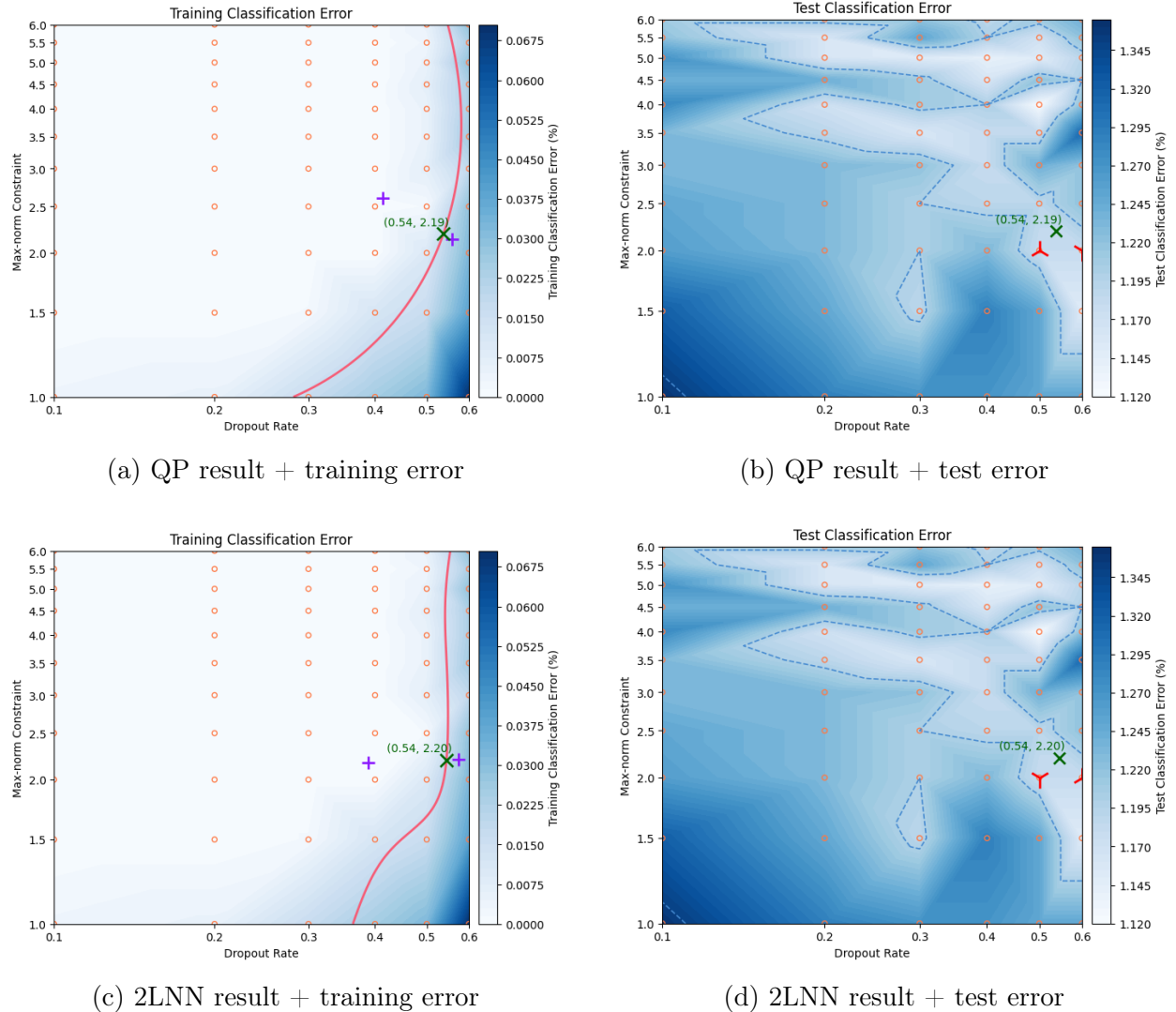


Figure 4: Classification error (in %) on the MNIST dataset as a function of the dropout rate  $r$  and the max-norm parameter  $c$ ; see Table 3.

The left side of Figure 4 shows the classification error (in %) on the training examples as the dropout parameter  $r$  (Step 2 of Table 3) and the max-norm parameter  $c$  (Step 4 of Table 3) vary over a “critical range”. The training error starts relatively low in the top-left corner when  $r$  is small and  $c$  is large, but the resulting networks in that region are likely overfitting the training data. As we gradually increase  $r$  and decrease  $c$ , the training error increases, slowly at first but more abruptly “at some point”.

Also shown on the left side of the figure are the boundaries marking the beginning of these abrupt increases as determined by our method, when the boundary itself is parameterized either as a QP (Figure 4a) or as a 2LNN (Figure 4c). Using either parameterization, our method suggests a dropout rate of no more than about  $r = 0.55$  and a max-norm parameter of no less than about  $c = 2.0$ ; it also finds an almost identical representative boundary point at roughly  $(r_b, c_b) = (0.54, 2.2)$ , labeled “ $\times$ ” in Figure 4 throughout.

The right side of Figure 4 shows the classification error (again, in %) on the 10,000 test examples. As is always the case, the overall performance landscape is much noisier on the test data. The reaffirming observation here is that the representative boundary point at roughly  $(r_b, c_b) = (0.54, 2.2)$  does indeed lie in a region of relatively low test error. Although a neural network has not been trained with this particular combination (i.e., a dropout rate of 0.54 and a max-norm parameter of 2.2), among those already trained the “nearest” one is at  $(r_b^\dagger, c_b^\dagger) = (0.5, 2.0)$ —labeled “ $\prec$ ” in Figure 4b and “ $\succ$ ” in Figure 4d; it has a competitive low test error of about 1.18%.

## 4 Discussion

We now make a few general observations and remarks.

First, the difference between the two parameterizations of the boundary (Section 2.5) is well within expectation: the QP parameterization (Section 2.5.1) gives rise to boundaries that are highly regular, convex, and quadratic, while the 2LNN parameterization (Section 2.5.2) leads to boundaries that are more flexible, but also more irregular, and not necessarily convex. However, despite these differences in appearance, in terms of dividing the points  $\{\mathbf{u}_1, \mathbf{u}_2, \dots, \mathbf{u}_n\}$  into two regions the two types of boundaries are still in high agreement with each other. The level of agreement between the two parameterizations is even higher when it comes to the representative boundary point (Section 2.6.1). This is also meant as the default answer of our method; in other words, it is our method’s automatic choice of the hyper-parameters. As such, it is worth noting that this choice also often turns out to be a practically good one.

Next, the choice of  $f(z; \boldsymbol{\theta}_j)$  simply as Gaussian with a common variance for  $j \in \{1, 2\}$  is inherited from the parent work (Zhu and Ghodsi, 2006) of this project, and we have noted earlier in Section 2.4 that it is quite arbitrary. But any method will naturally work well when its assumption is satisfied, however arbitrary the assumption may be. In our case, this will

happen if Eq. (7) is a reasonably good model for  $z_1, z_2, \dots, z_n$ . We have found this to be the case usually, if one focuses correctly on the critical region of the hyper-parameters where the model performance is changing the most, but poorly focused searches (of hyper-parameters) can certainly cause  $z_1, z_2, \dots, z_n$  to deviate severely from such an assumption and reduce the method’s effectiveness as a result.

Finally, readers may have noticed that, in Section 3, our  $z_1, z_2, \dots, z_n$  were often simply training performances at different hyper-parameter configurations, rather than properly cross-validated performances. While this clearly saves the amount of computation needed, our method is also particularly conducive to such practical shortcuts because, instead of aiming for configurations which optimize model performance, our method aims for configurations “at which improvements in model performance can be considered to have plateaued”. In the former context, only model performances measured independently of the training data are meaningful; whereas, in the latter, model performances measured on the training data itself can be meaningful, too.

## 5 Other applications

We end by noting that, in addition to hyper-parameter selection, we may also encounter other practical instances where “a boundary in the space of [explanatory variable  $\mathbf{u}$ ] at which [changes in a certain target variable  $z$ ] can be considered to have plateaued” is of direct interest. For example, surely we would all be happier with more wealth and freedom, but it is also conceivable that their marginal effects on our happiness will likely diminish beyond a certain point, and we may be interested in where such a boundary lies.

As an illustration of this phenomenon, we single out three national-level variables from the most recent World Happiness Report (Helliwell et al., 2025, Figure 2.1): for happiness, we use the three-year average national response to a Gallup World Poll (GWP) question about life evaluation; for wealth, we use log-GDP per capita; and for freedom, we use the average national response to a GWP question about freedom to make life choices. The latter two variables—about wealth and freedom—have both been rescaled by the authors of the report; for details about the nature of their rescaling, refer to various parts of Helliwell et al. (2025), e.g., their Box 2.1, Table 2.1, Box 2.2, and Chapter 2 Statistical Appendix. These three variables from a total of 144 countries (see Appendix C) are plotted in Figures 5a and 5b, together with the boundaries identified by our method. The boundaries clearly indicate that, while a country’s GDP must reach a certain threshold for its citizens’ life evaluation to be among the leading group, a wider perception of freedom to choose can, in fact, lower this threshold.

A more classic example is provided by Box et al. (2005, pp. 395–396), who described a small experimental study of harmful emissions from automobile engines. The amount of carbon monoxide (CO) emission was measured against two design variables: added ethanol and air-to-fuel ratio (AFR), each at three levels—low (−1), medium (0), and high (+1). The data

here generally point to a very strong interaction between the two: CO emission is highest when *both* the ethanol level is high *and* the AFR is low, and lowest when *either* the ethanol level is low *or* the AFR is high. This was confirmed by their Figure 11.17 (Box et al., 2005, p. 466), and is also evident from our Figures 5c and 5d, where the boundaries identified by our method, at which drops in CO emission can be considered to have stabilized, are also shown.

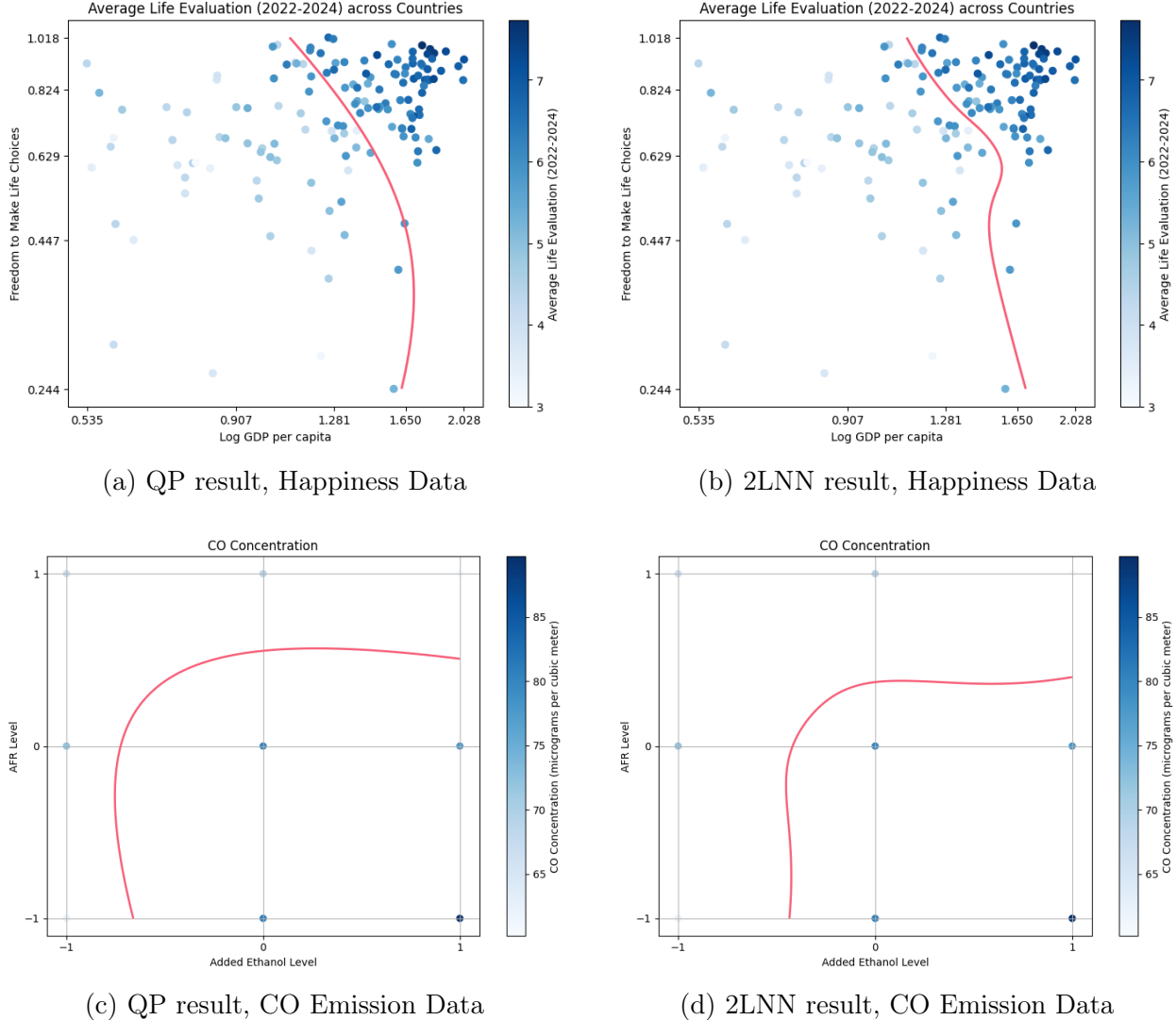


Figure 5: Applications of our method to other data-analytic tasks—top, happiness as a function of wealth and freedom; bottom, carbon monoxide (CO) emission as a function of added ethanol and air-to-fuel ratio (AFR).

A few remarks we made in Section 4 are worth reiterating. First, the boundaries have different appearances depending on how they are parameterized (QP versus 2LNN), but they agree in terms of how the space should be divided—here, into two regions of high versus low life evaluations, and of high versus low CO emission. Next, the main reason why

our method works well here is, again, driven mostly by the fact that Eq. (7) turns out to be a reasonably good model for these data (see Figure 6 in Appendix C). While we believe this can hold in some other practical applications too, we certainly do not anticipate it to hold universally for all potential applications. However, in principle one is free to make a different model assumption in Eq. (7) and still apply our methodology to find the desired boundary by maximizing the softened profile log-likelihood (5).

## A Derivation of Eq. (8)

In this appendix we show that, under assumption (7), Eq. (5) can be further reduced to Eq. (8). First, it is elementary to establish that, under assumption (7) with  $\boldsymbol{\theta}_j \equiv (\mu_j, \sigma^2)$  for  $j \in \{1, 2\}$ , the solutions to (6) while fixing  $\boldsymbol{\omega}$  are given by

$$\hat{\mu}_1(\boldsymbol{\omega}) = \frac{\sum_{i=1}^n (1 - s_i(\boldsymbol{\omega})) z_i}{\sum_{i=1}^n (1 - s_i(\boldsymbol{\omega}))}, \quad \hat{\mu}_2(\boldsymbol{\omega}) = \frac{\sum_{i=1}^n s_i(\boldsymbol{\omega}) z_i}{\sum_{i=1}^n s_i(\boldsymbol{\omega})}, \quad \hat{\sigma}^2(\boldsymbol{\omega}) = \frac{\text{RSS}_1(\boldsymbol{\omega}) + \text{RSS}_2(\boldsymbol{\omega})}{n},$$

where

$$\text{RSS}_1(\boldsymbol{\omega}) = \sum_{i=1}^n (1 - s_i(\boldsymbol{\omega})) (z_i - \hat{\mu}_1(\boldsymbol{\omega}))^2, \quad \text{RSS}_2(\boldsymbol{\omega}) = \sum_{i=1}^n s_i(\boldsymbol{\omega}) (z_i - \hat{\mu}_2(\boldsymbol{\omega}))^2.$$

Plugging these back into Eq. (5), we now get

$$\begin{aligned} \ell_{\boldsymbol{\omega}}^{\text{soft}}(\boldsymbol{\omega}) &= \sum_{i=1}^n (1 - s_i(\boldsymbol{\omega})) \log f(z_i; \hat{\boldsymbol{\theta}}_1^{\text{soft}}(\boldsymbol{\omega})) + \sum_{i=1}^n s_i(\boldsymbol{\omega}) \log f(z_i; \hat{\boldsymbol{\theta}}_2^{\text{soft}}(\boldsymbol{\omega})) \\ &= \sum_{i=1}^n (1 - s_i(\boldsymbol{\omega})) \log \left\{ \frac{1}{\sqrt{2\pi\hat{\sigma}^2(\boldsymbol{\omega})}} \exp \left\{ -\frac{(z_i - \hat{\mu}_1(\boldsymbol{\omega}))^2}{2\hat{\sigma}^2(\boldsymbol{\omega})} \right\} \right\} + \\ &\quad \sum_{i=1}^n s_i(\boldsymbol{\omega}) \log \left\{ \frac{1}{\sqrt{2\pi\hat{\sigma}^2(\boldsymbol{\omega})}} \exp \left\{ -\frac{(z_i - \hat{\mu}_2(\boldsymbol{\omega}))^2}{2\hat{\sigma}^2(\boldsymbol{\omega})} \right\} \right\} \\ &= \sum_{i=1}^n (1 - s_i(\boldsymbol{\omega})) \left\{ -\frac{1}{2} \log(2\pi\hat{\sigma}^2(\boldsymbol{\omega})) - \frac{(z_i - \hat{\mu}_1(\boldsymbol{\omega}))^2}{2\hat{\sigma}^2(\boldsymbol{\omega})} \right\} + \\ &\quad \sum_{i=1}^n s_i(\boldsymbol{\omega}) \left\{ -\frac{1}{2} \log(2\pi\hat{\sigma}^2(\boldsymbol{\omega})) - \frac{(z_i - \hat{\mu}_2(\boldsymbol{\omega}))^2}{2\hat{\sigma}^2(\boldsymbol{\omega})} \right\} \\ &= -\frac{1}{2} n \log(2\pi\hat{\sigma}^2(\boldsymbol{\omega})) - \\ &\quad \frac{1}{2\hat{\sigma}^2(\boldsymbol{\omega})} \left\{ \sum_{i=1}^n (1 - s_i(\boldsymbol{\omega})) (z_i - \hat{\mu}_1(\boldsymbol{\omega}))^2 + \sum_{i=1}^n s_i(\boldsymbol{\omega}) (z_i - \hat{\mu}_2(\boldsymbol{\omega}))^2 \right\} \\ &= -\frac{1}{2} n \log(2\pi\hat{\sigma}^2(\boldsymbol{\omega})) - \frac{1}{2\hat{\sigma}^2(\boldsymbol{\omega})} \{ \text{RSS}_1(\boldsymbol{\omega}) + \text{RSS}_2(\boldsymbol{\omega}) \} \end{aligned}$$

$$= -\frac{n}{2} \log(2\pi\hat{\sigma}^2(\boldsymbol{\omega})) - \frac{n}{2},$$

which is Eq. (8).

## B Details of the MNIST example in Section 3.3

For the MNIST data, each input is a  $28 \times 28$  image represented as  $\mathbf{x} \in \mathbb{R}^{784}$  ( $28 \times 28 = 784$ ). The neural network architecture used in Section 3.3 is one considered by Srivastava et al. (2014) with two hidden layers, each consisting of 2048 nodes; thus,

$$\begin{aligned}\mathbf{W}_1 &\in \mathbb{R}^{2048 \times 784}, & \mathbf{b}_1 &\in \mathbb{R}^{2048}, \\ \mathbf{W}_2 &\in \mathbb{R}^{2048 \times 2048}, & \mathbf{b}_2 &\in \mathbb{R}^{2048}, \\ \mathbf{W}_3 &\in \mathbb{R}^{10 \times 2048}, & \mathbf{b}_3 &\in \mathbb{R}^{10}.\end{aligned}$$

### B.1 Details about dropout

Following Srivastava et al. (2014), we only study the impact of the dropout rate  $r$  used for the hidden layers, while for the input layer the dropout rate is fixed at 0.2. The exact specification of our dropout operator  $\mathbb{D}(\cdot; r)$ , when applied to Eq. (15), is:

$$\mathbb{D}(\mathbf{p}(\mathbf{x}); r) = \sigma [\mathbf{W}_3 D_r \{ \rho(\mathbf{W}_2 [D_r \{ \rho(\mathbf{W}_1 [D_{0.2}(\mathbf{x})] + \mathbf{b}_1) \}] + \mathbf{b}_2) \} + \mathbf{b}_3],$$

where

$$D_r(\mathbf{z}) = \frac{\mathbf{1}_r \odot \mathbf{z}}{1 - r};$$

$\mathbf{1}_r$  is an i.i.d. vector drawn element-wise from the  $\text{Bernoulli}(1 - r)$  distribution; and “ $\odot$ ” denotes element-wise multiplication. That is,  $D_r(\mathbf{z})$  randomly annihilates some elements of  $\mathbf{z}$  by turning them into zeros, and rescales the rest by one minus the dropout rate, so that its output is equal *in expectation* to its input:

$$\mathbb{E}(D_r(\mathbf{z})) = \frac{\mathbb{E}(\mathbf{1}_r \odot \mathbf{z})}{1 - r} = \mathbf{z}.$$

### B.2 Other details

For the MNIST data, the stochastic gradient descent algorithm in Table 3 initializes the vectors  $\mathbf{b}_1, \mathbf{b}_2, \mathbf{b}_3$  to  $\mathbf{0}$ , and draws the initial weight matrices

$$\mathbf{W}_1 \sim \mathcal{N}\left(0, \frac{1}{\sqrt{784}}\right), \quad \mathbf{W}_2, \mathbf{W}_3 \sim \mathcal{N}\left(0, \frac{1}{\sqrt{2048}}\right)$$

element-wise from scaled normals, all centered at zero. Furthermore, it uses

- a total of  $T = 1,000,000$  iterations;
- a mini-batch size of  $B = 100$ ;
- a momentum schedule of

$$\mu_t = \begin{cases} 0.9 + 0.05 \cdot (t-1)/10,000, & t \leq 10,000, \\ 0.95, & t > 10,000; \end{cases}$$

- and a learning-rate schedule of

$$\epsilon_t = \epsilon_0 \cdot \gamma^{t-1} \quad \text{with} \quad \epsilon_0 = 0.01 \quad \text{and} \quad \gamma = 0.5^{1/10,000}.$$

## C Details of other applications in Section 5

For the year of 2024, the data set from Helliwell et al. (2025, Figure 2.1) contains life evaluations for 147 countries. Three countries—Afghanistan, Tajikistan and Venezuela—have been omitted from Figures 5a and 5b, because their “GDP variable” or “freedom variable” is either missing or has been rescaled by the authors to 0.000, which prevents us from applying the logarithmic transform prior to optimization (see Section 2.6.2).

Figure 6 shows that Eq. (7) is not a grossly inappropriate model for the “happiness” data despite a noticeable second mode in the distribution on the left, and that it is even a pretty good one for the “CO emission” data.

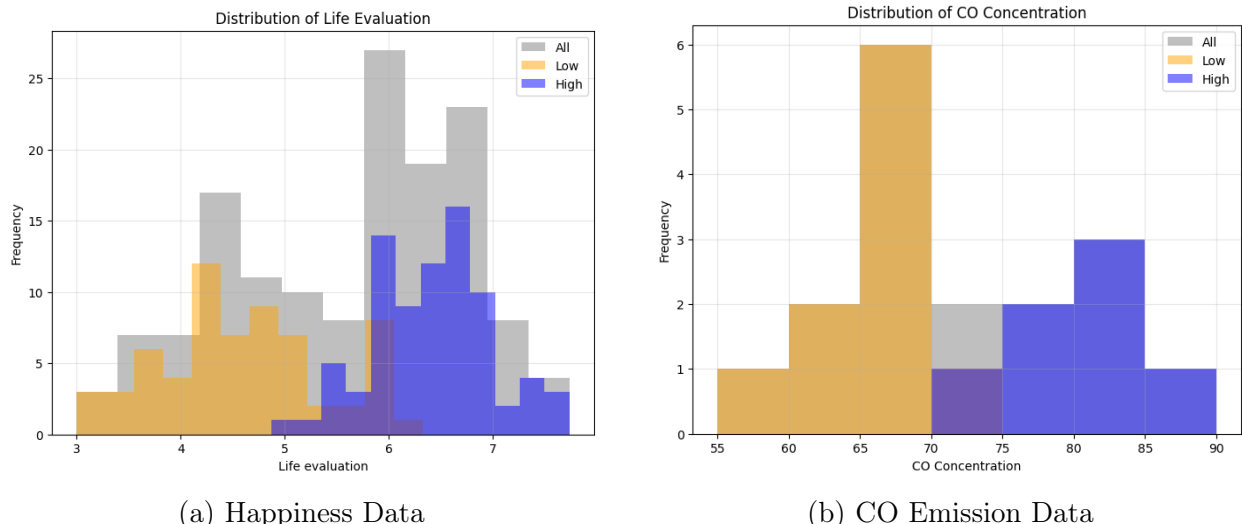


Figure 6: Distribution of the target variable—life evaluation (6a) and CO concentration (6b)—on either side of the boundary (Figure 5).

## References

Box, G. E. P., Hunter, J. S., and Hunter, W. G. (2005). *Statistics for Experimenters: Design, Innovation, and Discovery*. Wiley, 2nd edition.

Chang, M.-C., Tung, C.-H., Chang, S.-Y., Carrillo, J. M., Wang, Y., Sumpter, B. G., Huang, G.-R., Do, C., and Chen, W.-R. (2022). A machine learning inversion scheme for determining interaction from scattering. *Communications Physics*, 5:46.

Cortes, C. and Vapnik, V. (1995). Support-vector networks. *Machine Learning*, 20:273–297.

Fogel, P., Young, S. S., Hawkins, D. M., and Ledirac, N. (2007). Inferential, robust non-negative matrix factorization analysis of microarray data. *Bioinformatics*, 23(1):44–49.

Hamady, M., Lozupone, C., and Knight, R. (2010). Fast UniFrac: facilitating high-throughput phylogenetic analyses of microbial communities including analysis of pyrosequencing and PhyloChip data. *The ISME Journal: Multidisciplinary Journal of Microbial Ecology*, 4(1):17–27.

Helliwell, J. F., Layard, R., Sachs, J. D., De Neve, J.-E., Aknin, L. B., and Wang, S., editors (2025). *World Happiness Report 2025*. University of Oxford: Wellbeing Research Centre.

Honarkhah, M. and Caers, J. (2010). Stochastic simulation of patterns using distance-based pattern modeling. *Mathematical Geosciences*, 42(5):487–517.

Jian, J., Sang, P., and Zhu, M. (2024). Two Gaussian regularization methods for time-varying networks. *Journal of Agricultural, Biological and Environmental Statistics*, 29:853–873.

Kingma, D. P. and Ba, J. (2014). ADAM: A method for stochastic optimization. *arXiv preprint arXiv:1412.6980*.

Lai, C.-Q., Tucker, K. L., Choudhry, S., Parnell, L. D., Mattei, J., García-Bailo, B., Beckman, K., Burchard, E. G., and Ordovás, J. M. (2009). Population admixture associated with disease prevalence in the Boston Puerto Rican health study. *Human Genetics*, 125:199–209.

Lyzinski, V., Tang, M., Athreya, A., Park, Y., and Priebe, C. E. (2017). Community detection and classification in hierarchical stochastic blockmodels. *IEEE Transactions on Network Science and Engineering*, 4(1):13–26.

Nocedal, J. and Wright, S. J. (2006). *Numerical Optimization*. Springer Series in Operations Research and Financial Engineering. Springer New York, NY, 2 edition.

Priebe, C. E., Park, Y., Vogelstein, J. T., Conroy, J. M., Lyzinski, V., Tang, M., Athreya, A., Cape, J., and Bridgeford, E. (2019). On a two-truths phenomenon in spectral graph clustering. *Proceedings of the National Academy of Sciences*, 116(13):5995–6000.

Sakar, B. E., Isenkul, M. E., Sakar, C. O., Sertbas, A., Gurgen, F., Delil, S., Apaydin, H., and Kursun, O. (2013). Collection and analysis of a Parkinson speech dataset with multiple types of sound recordings. *IEEE Journal of Biomedical and Health Informatics*, 17(4):828–834.

Srivastava, N., Hinton, G., Krizhevsky, A., Sutskever, I., and Salakhutdinov, R. (2014). Dropout: A simple way to prevent neural networks from overfitting. *Journal of Machine Learning Research*, 15(56):1929–1958.

Tang, M., Athreya, A., Sussman, D. L., Lyzinski, V., Park, Y., and Priebe, C. E. (2017). A semiparametric two-sample hypothesis testing problem for random graphs. *Journal of Computational and Graphical Statistics*, 26(2):344–354.

Zhong, F., Rosenberg, M., Agterberg, J., and Crabb, R. (2021). Social determinant-based profiles of U.S. adults with the highest and lowest health expenditures using clusters. *North American Actuarial Journal*, 25(1):115–133.

Zhu, M. and Ghodsi, A. (2006). Automatic dimensionality selection from the scree plot via the use of profile likelihood. *Computational Statistics & Data Analysis*, 51(2):918–930.

Zou, H. and Hastie, T. J. (2005). Regularization and variable selection via the elastic net. *Journal of the Royal Statistical Society, Series B*, 67(2):301–320.